PROCEEDINGS OF SPIE

A sounding rocket payload for x-ray observations of the Cygnus Loop

Randall L. McEntaffer, Webster Cash, Ann Shipley, Eric Schindhelm

SPIE.

A sounding rocket payload for X-ray observations of the Cygnus Loop

Randall L. McEntaffer[*], Webster Cash, Ann Shipley & Eric Schindhelm

University of Colorado, Center for Astrophysics and Space Astronomy, 593 UCB,

1255 38th St, Boulder, CO 80309-0593

ABSTRACT

We present a new sounding rocket payload that will perform high resolution (R~100) x-ray spectroscopy of diffuse celestial x-ray sources. The instrument features a new geometry that allows for high resolution along with high throughput. A wire grid collimator constrains light from diffuse sources into a converging beam that feeds an array of diffraction gratings in the extreme off-plane mount. Starting with launch in 2006 we can obtain physical diagnostics of supernova remnants such as the Cygnus Loop and ultimately the hot phase of the interstellar medium.

Keywords: Sounding rocket, diffuse x-ray spectroscopy, off-plane mount, Cygnus Loop

1. INTRODUCTION

Currently there is no efficient, well developed technology that permits high resolution x-ray spectroscopy from large solid angle sources, making spectra of diffuse x-ray sources rare. The few existing spectra have established there is a rich trove of science waiting. With our instrument we can address the structure and dynamics of supernova remnants and the hot phase of the interstellar medium. Furthermore, we can obtain physical diagnostics of the galactic halo and possibly even detect emission from the intergalactic medium.

We propose to employ a diffraction grating array in the extreme off-plane mount. This technology provides a major advance in capability for the x-ray spectroscopist. For diffuse source spectroscopy it provides a path to efficient high resolution spectroscopy that simply cannot be supported by calorimeters or in-plane gratings. The off-plane mount provides a natural geometry for grazing incidence grating arrays and has the potential to become the technology of choice for high resolution missions.

The flood of high quality data from the Chandra and XMM-Newton Observatories, makes it clear that high resolution dispersive spectroscopy is a key component of x-ray astronomy and will be around for the long term. The Constellation-X mission recognizes this need by including a Reflection Grating Spectrometer in its instrument array. However, there is a widely perceived need to improve the baseline resolution of the Con-X RGS. The off-plane mount is now being studied by the Con-X team and the projected capability looks good. This rocket payload will provide the test bed for off-plane grating technology from conceptual design through flight to data analysis and publication.

The first flight for this payload is scheduled for launch at White Sands Missile Range on September 7, 2006. During this flight we will obtain a soft x-ray spectrum of the entire Cygnus Loop supernova remnant. Subsequent flights are planned for the fall of 2008 and 2009 to observe the soft x-ray background.

2. SCIENCE OBJECTIVES

The scientific goal of this proposed sounding rocket is to obtain spectral diagnostics of nearby extended supernova remnants such as the Cygnus Loop and of the soft x-ray background. Results to date in this area have been extremely limited, despite the obvious importance to understanding the nature and dynamics of the local interstellar medium and the galactic halo. In this section we review the scientific rationale that drives the need for the kind of spectra that our proposed instrument can acquire.

The Cygnus Loop is the quintessential middle aged, shell structured supernova remnant. It covers a large patch of sky (2.8º × 3.5º), has low extinction[1], E(B-V)=0.08 and is close by at a distance of 540pc[2]. The morphology of this remnant results when the shock wave from the supernova blast encounters a shell of inhomogeneous medium. Interactions of this shock wave with clouds present in this structure create emission that dominates at all wavelengths including X-rays. The

[*] randall.mcentaffer@colorado.edu; phone 1 303 492-5835; fax 1 303 492-5941

shell morphology is consistent with the idea of cavity explosion[3] where the progenitor star wind pushes out ambient medium to create a cavity in which the supernova occurs. We are now seeing the blast wave catch up to the outlying material.

The first flight of the payload will concentrate on the Cygnus Loop and has been designated the Cygnus X-ray Emission Spectroscopic Survey (CyXESS)[4]. This will not only provide valuable scientific data for supernova remnants but will also serve as a proof of concept flight for subsequent missions. Following the successful retrieval of the CyXESS payload a second flight will launch to study the X-ray background. CyXESS will provide the first high resolution spectrum in the soft X-ray band (0.1-0.7keV). High resolution observations of the Cygnus Loop have been made for OVII (561-574eV) and OVIII (653eV)[5], but not of the spectrum as a whole and more importantly not at lower energies. These lower energies are important because it has been found that the X-ray emission from the Cygnus Loop is dominated by the soft X-ray component[6,7,8]. The high spectral resolution will allow us to perform nonequilibrium model fits at a higher accuracy than ever before to determine plasma characteristics. The spectrum will be of the entire remnant but in the case of the Cygnus Loop will originate from a spatially limited area[6,8,9] and be indicative of a specific interaction between the supernova blast wave and clouds in the ambient shell as seen in figure 1.
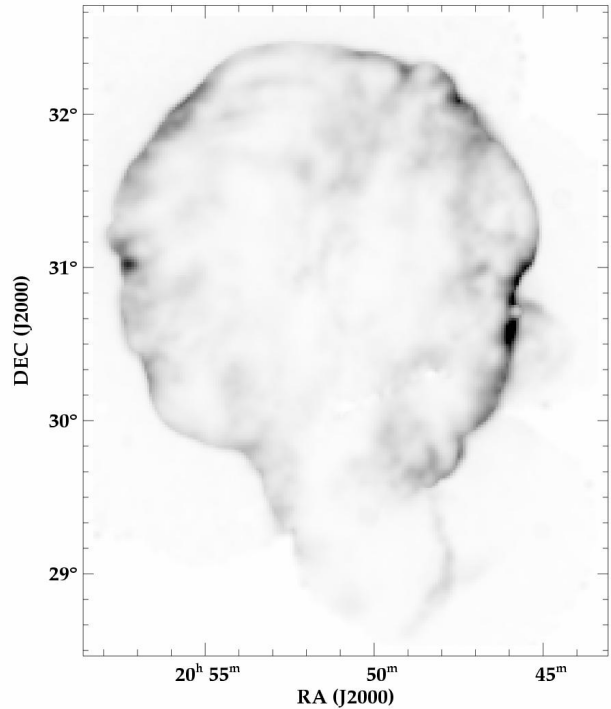

Figure 1: Cygnus Loop soft x-ray emission[6].

One of the line ratios that tells us something about the physics of the plasma is the OVIII/OVII ratio. The relative density of ions in each of these states shows what stage of ionization the plasma is in. This density relation can be found from the flux ratio of the two lines using the following equation

$$\frac{f_{ig}}{f_{jk}} = \frac{n_{Z^{+z}}\Omega_{ig}}{n_{Z^{+x}}\Omega_{jk}}\exp\left[-\left(E_{ig}-E_{jk}\right)/kT\right]\exp\left[-\left(\sigma_{ig}-\sigma_{jk}\right)/N_H\right] \quad (1)$$

where $i{\rightarrow}g$ and $j{\rightarrow}k$ are transitions in the different ions, f is flux, Ω is the effective collision strength, σ is the interstellar absorption cross section and n is the ion density. The exponential terms are of order 1 for transitions with similar energies. Even if this is not the case then the temperature and column density can be found from equilibrium or nonequilibrium models. This test can also be performed on the SiIX and SiX lines that are expected at 225eV and 250eV.

Another informative line ratio can be found within He-like ions. The helium isosequence of oxygen forms a triplet of lines, a resonance line (R) at 574eV, an intercombination line (I) at 569eV and a forbidden line (F) at 561eV. The F/R ratio is important to measure because it is dependent on the ionization state of the gas. In an equilibrium plasma these lines can be formed through collisions, ionizations of Li-like ions or recombinations of H-like ions. The recombination of H-like ions strengthens the contribution from the forbidden transition due to its larger statistical weight. However, as a blast wave ionizes a medium the ions obtain a higher temperature than the electrons and until the electron temperature equilibrates the gas remains underionized. Therefore, the number of H-like ions in an ionizing medium is depleted compared to the equilibrium case. This in turn causes the F/R ratio to be much lower during the early ionization stages than when the gas has reached equililbrium. For equilibrium plasmas around 10^6K the F/R ratio is around 1 and can fall to 0.6 at temperatures of 10^7K. Therefore, a measure of the temperature combined with the F/R ratio will determine whether the gas is still ionizing or has reached equilibrium. Vedder et al.[5] used the Einstein Observatory to obtain a high resolution spectrum of the OVII, OVIII and NeIX emission lines of the Cygnus Loop (figure 2). They observed a bright region in the northern section of the remnant using a 3'×30' aperture. Small bandpasses around these lines were

observed for 61 kiloseconds to obtain the line spectra. They concluded that they observed no forbidden line emission at the 3σ level implying that the observed area was not yet in ionization equilibrium.

CyXESS will observe the entire remnant to determine if this is the trend overall. The radiation rate in a shocked cloud is $\propto n^2 \Lambda$ where n is the density and Λ is the recombination rate. In denser clouds the ion temperature will equilibrate with the electron temperature on a shorter time scale and consequently increase the F/R ratio. If the Vedder et al.

Figure2: Oxygen line spectrum from Vedder et al 1986.

observation was done in a region that's not indicative of the densest areas of the shell then a full scale observation will show detectable forbidden line strength. However, if CyXESS observes no forbidden line emission as well then we could conclude that the Cygnus Loop is currently in the early stages of blast wave interaction with the ambient medium and that it is still ionizing as a whole.

CyXESS will be the first instrument to provide a high resolution spectrum in the soft X-ray bandpass. As discussed above, the spectrum that CyXESS obtains of the Cygnus Loop as a whole will be dividable into contributions from the two temperature regions, the cloud shock and the reflected shock, which both originate from the interaction of the blast wave with clouds. In addition, the high spectral resolution will allow us to employ nonequilibrium model fits, which will determine electron temperature, column density, emission measure, ionization parameter and abundance determinations of elements such as O, Si, Fe, Ne and Mg. The fits will be more exact and allow a stricter constraint on the variables. The abundant number of lines achievable with this resolution will be indicative of many temperature ranges. By calculating the emission measure for each line, we will be able to estimate the emission measure as a function of temperature for the entire remnant.
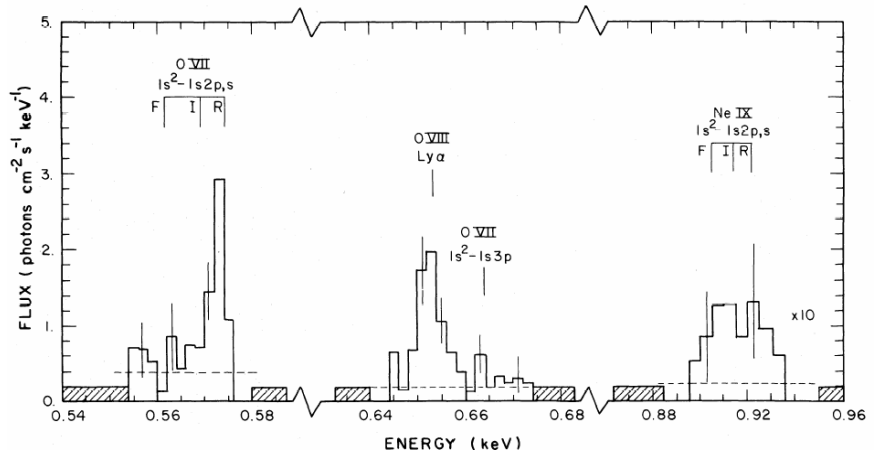
3. OFF-PLANE GEOMETRY

In college physics we were all introduced to diffraction gratings as a two-dimensional phenomenon as shown on the left in figure 3. The radiation is incident on the grating in the plane perpendicular to the direction of the grooves, and the diffracted light remains in that plane. When we move to grazing incidence, the value of the angle α must approach 90 degrees, and β will similarly remain near -90 degrees for a small change of angle and good efficiency in the x-ray. This is known as the in-plane mount, and was utilized in EUVE and XMM-Newton.

The off-plane mount at grazing incidence brings light onto the grating at a low graze angle, quasi-parallel to the direction of the grooves as shown on the right in figure 3[10,11]. The light is then diffracted through an arc, forming a cone, so that this mount is also known as conical diffraction. The grating equation is now

$$\sin \alpha + \sin \beta = \frac{n\lambda}{d \sin \gamma}.$$ (2)

where d is the spacing between grooves. γ is the angle between the direction of the incoming ray and the direction of the groove at the point of impact. Light comes into the grating at an azimuthal angle of α along a cone with half-angle γ. It is then diffracted along the same cone of half-angle γ, but now with an azimuthal angle of β.

While it is not at all evident at first glance, the off-plane mount is the natural geometry for grazing incidence reflection gratings, and with it we accrue a substantial set of advantages. Chief among these is the potential for higher resolution. Since the diffracted radiation emerges at the same (conical) angle at which it approaches, one may disperse through

twice the graze angle[10]. The in-plane mount disperses away from the reflected zero order, and thus can only disperse through about half the graze angle. A second advantage of the off-plane mount is dispersion to very high values of β to achieve extra resolution as in an echelle spectrograph[12]. Third, optical errors in fabrication and assembly create blurs that are almost entirely in the in-plane direction. Not only does this aid resolution but there is also a significant easing of fabrication tolerances because the off-plane disperses perpendicular to the direction of scatter. Furthermore, the packing geometries can be substantially better as discussed in Cash 1991[10].
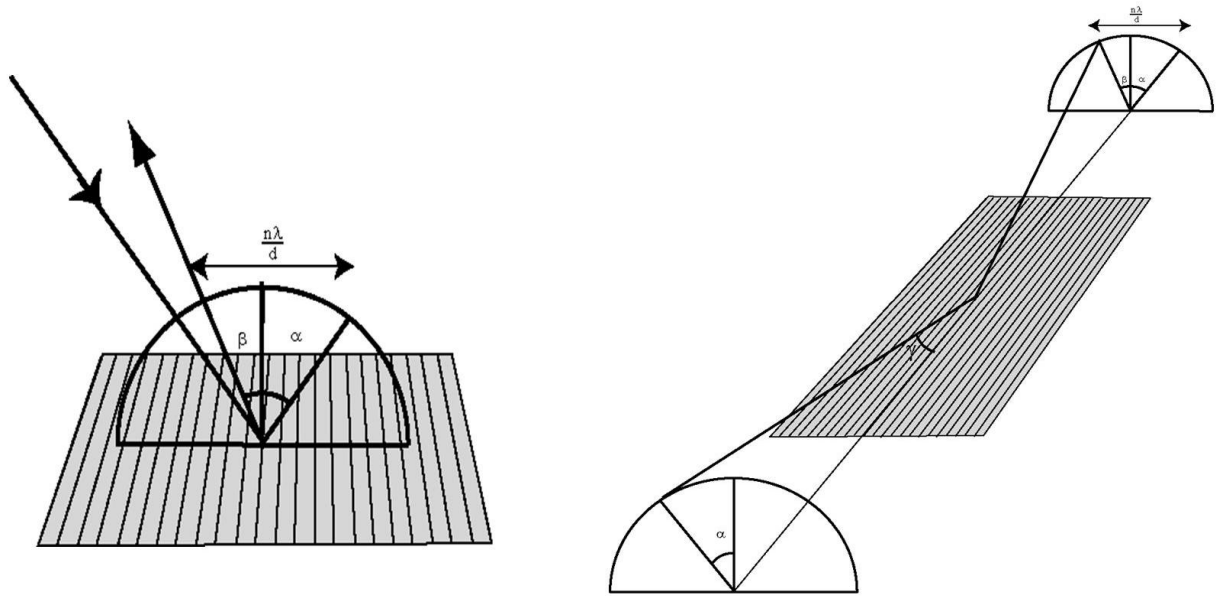

Fig. 3: Left: Geometry of the in-plane reflection. Both incident and diffracted light lie in the plane normal to the ruling direction. Right: Geometry of the off-plane mount. Light approaches the gratings quasi-parallel to the grooves. Diffracted light lies in a cone around the direction of the rulings.

The other key advantage gained by using the off-plane mount is diffraction efficiency. The effective diffraction efficiency of the off-plane mount can be substantially higher than traditional mounts (often a factor of two) due to the groove illumination function[13,14]. In the off-plane mount the effect of groove shadowing is lessened. Furthermore, rigorous efficiency calculations of blazed gratings show that the off-plane mount can have efficiencies up to 70% and on average a few times higher than efficiencies obtainable with a traditional in-plane grating mount[15].

We at the University of Colorado have already performed efficiency and resolution tests of high groove density gratings in the extreme off-plane mount[16,17]. Gratings have been fabricated by Jobin-Yvon with blazed high density grooves. The first efficiency tests of these gratings in the off-plane mount have provided some very promising numbers. Diffraction efficiencies at Carbon-K 0.277keV are 25% in diffracted orders and 46% total. For Oxygen-K 0.525keV the diffracted orders are 27.3% efficient and 49% total. At Mg-K 1.25keV the blazed grating had all of its light in diffracted orders with 40.5% efficiency. The unblazed grating at this energy had 40% in diffracted orders as well with an additional 7% in zero order. From this initial study we have obtained diffraction efficiencies up to 40% sum of orders under non-optimal conditions. We have also tested gratings fabricated at MIT[18]. These gratings produce similar if not better results and support the finding that the off-plane mount produces a high efficiency spectrometer.

The only substantive disadvantage of the off-plane mount is the need for higher groove density. In-plane diffraction requires a lower density of grooves because the values of α and β are near 90 degrees, and the grating equation is in a non-linear regime. Mechanically ruled high groove density gratings have traditionally had problems with low groove efficiency and high scatter. However, the state-of-the-art of diffraction gratings, i.e. holographic ruling and ion etching, provides the needed high groove densities. Densities around 6000g/mm are standard and are being flown on both FUSE and COS.

4. PAYLOAD DESIGN

4.1 Overall payload design

The purpose of our payload is to observe diffuse x-ray sources in the soft x-ray (0.1-0.7keV). A relatively bright source like the Cygnus Loop provides a good source of x-rays within a workable field of view (FOV). Using optics like nested Wolter telescopes is expensive, heavy and unattractive for a rocket flight. We found that a wire grid collimator offers an inexpensive method to focus x-rays (see section 4.2). The collimator will be followed by the off-plane reflection grating array (section 4.3) and finally the detectors (section 4.4). The payload will be three meters long consisting of nearly a meter to create the converging beam and allowing the gratings to throw the light about two meters to the detectors. The Cygnus Loop can be covered by a 3.25° x 3.25° FOV. This opening angle over 3m gives us an aperture opening of 170mm or 6.7" at the front of the payload. Using the optimal packing geometry for a 22" payload skin we were able to fit 6 telescopes or "modules" into the payload as shown in figure 4. The optimal packing geometry results in an octagonal FOV, within which the Cygnus Loop x-ray emission fits, and defines the layout of the entire payload. Due to budget constraints we will design the payload for 6 modules but only fill two of these with components. For symmetry, two opposing modules were chosen. A generic light path through the payload with two modules is shown in figure 5.
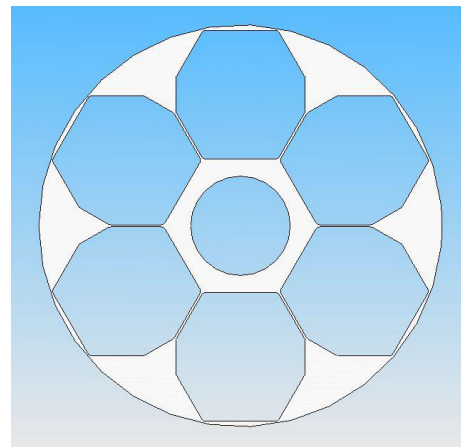

Figure 4: Packing geometry for the 6 modules within a 22" rocket skin. The hole in the center is for the star tracker.

4.2 Collimator design

The signal one captures with a diffuse object spectrograph depends on the grasp of the system, which is measured in $cm^2 \cdot steradian \cdot seconds$. In a rocket flight, the number of seconds is limited, so one must emphasize either effective area or solid angle. Effective area gives one sensitivity to small targets, and steradians are effective only when observing very large targets. We have decided to build a system that has a very large solid angle of response, but low effective collecting area. This eliminates the need for an expensive and probably inefficient telescope.

A conventional wire grid collimator features wires that are spaced periodically in such a way that only light coming from a specified direction can pass through. However, as shown schematically in Figure 6, if the grids have a spacing that decreases systematically, then it is possible to allow only light that is converging to a point to pass through, simulating the output of a lens. As light travels from front to back in the collimator it will encounter the same number of slits but they'll be narrower and closer together, thus sculpting the converging beam. The wires create baffles between slits which vignette unwanted rays. If thin material is used, these wire spacers serve as knife edges so that any light striking the metal will be near normal incidence and will be efficiently absorbed. Such a collimator would not
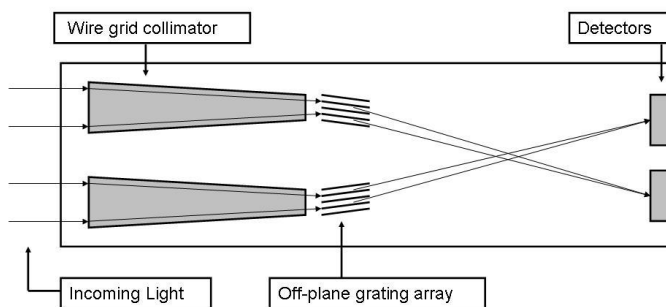

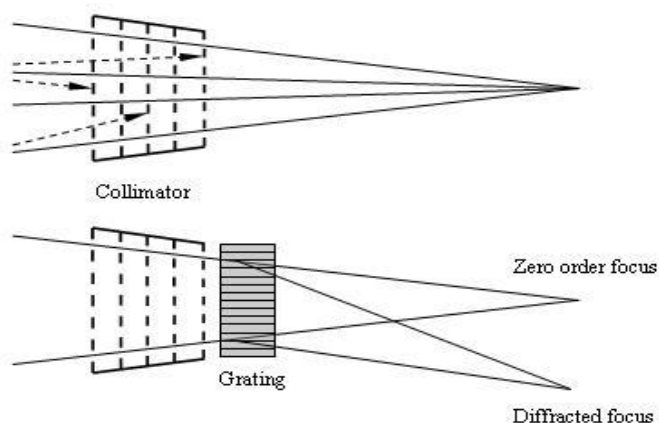Figure 5: Schematic of the light path through the payload.

Figure 6: On the top, a schematic of a wire grid collimator illustrates how only converging light will be allowed through. The drawing on the bottom shows how a grating placed in this cone of light will produce a focused spectrum.

function well for a point source, but for a diffuse target, radiation comes from all directions, and the beam would be fully illuminated. A grating mounted in the beam would diffract just as in a telescope beam. Thus the collimator alone provides the needed beam geometry.
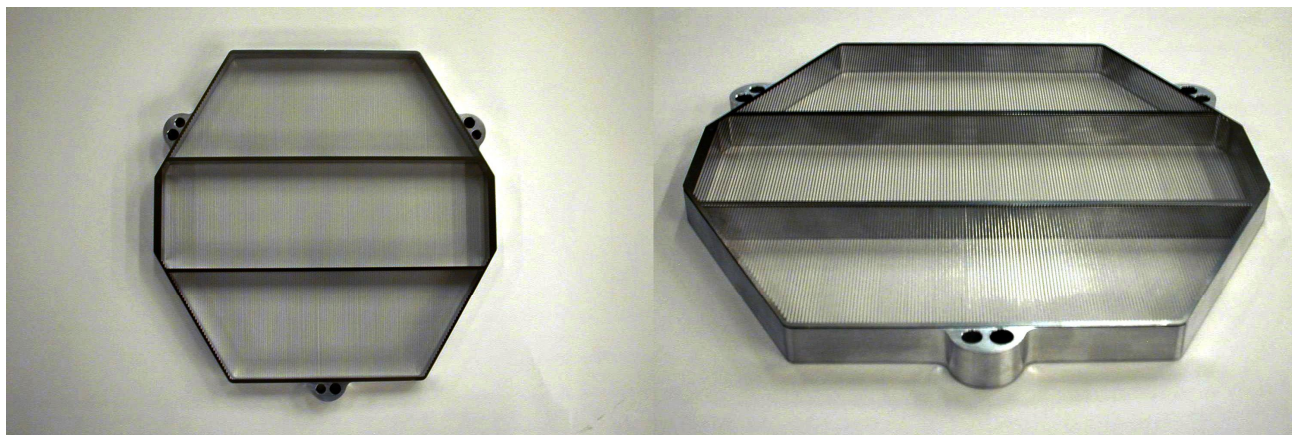

Figure 7: On the left, a typical collimator plate. On the right, the same plate at an angle to show detail in the spacers and slits.

Figure 7 shows a photograph of a collimator plate. The size and shape of the plate were chosen to match the octagonal module openings seen in figure 4. Each collimator plate consists of a frame that holds a sheet (0.005" thick) of stainless steel into which a pattern of slits is cut. Precise slit spacing for each sheet was modeled and drawn in SolidWorks. A lithograph of the part is made from the model to form a mask for the sheet. Acid is then applied to the mask to etch out the unwanted material leaving the desired pattern of slits and spacers. Limitations on this etching process define the smallest spacer achievable while desired line width (resolution) defines the necessary slit width. These factors translate into a spacer width of 114μm and a slit width of 500μm for the final sheet in the stack. The desired field of view requires these numbers to increase to a spacer width of 166μm and a slit width of 725μm for the front sheet in the collimator. As is evident in figure 7, the slits only cause a converging beam in one dimension (perpendicular to the slits) while leaving the other dimension (along the slits) virtually untouched. This results in lines of light coming from each slit that are long and thin. Due to the convergence of the beam, these slit images overlap at the focus.

Defining the slit and spacer widths at the front and the back of the collimator was easy using simple geometry. However, efficiently filling the space between them with collimator plates was not trivial. We needed to minimize the number of plates used due to cost and space available while ensuring that the amount of light outside the desired beam be kept to a minimum as well. Raytracing the collimator showed that the optimal converging beam was formed using 46 collimator plates. This would keep all of the light in the focused beam but would be impossible to implement because of the extremely close proximity of plates in the front of the collimator (2mm) and the impractical difference between slit width sizes for these plates (1nm). We found that we could remove 22 of these plates and still keep the amount of light outside the beam to <5%. Removing any more caused the stray light to increase by a couple percent per plate removal. This results in a total of 24 collimator plates. The positions relative to one another in the collimator are shown in Figure 8.

The assembly shown in figure 8 consists of 6 aluminum support tubes that are welded to 13 "skeleton" plates onto which the collimator plates are mounted. The spacing between collimator plates will be kept by the precision welded assembly. This figure also shows the alignment fixture. A set of 5 lasers are aligned to go through the collimator in a converging beam matching that of the field of view. Each collimator plate is then placed onto its respective skeleton plate and aligned to these lasers. When aligned the plates are held in place by three screws and three potted pins. An engineering test unit was made to analyze the effects of a vibration test on the alignment of the first 9 collimator plates. After initial alignment of the first nine plates using the same laser alignment method described above, we measured the X-ray throughput and performed the vibration test at Ball Aerospace. After shake we confirmed that neither the laser alignment nor the X-ray throughput had changed thus verifying that the structure was good for flight.
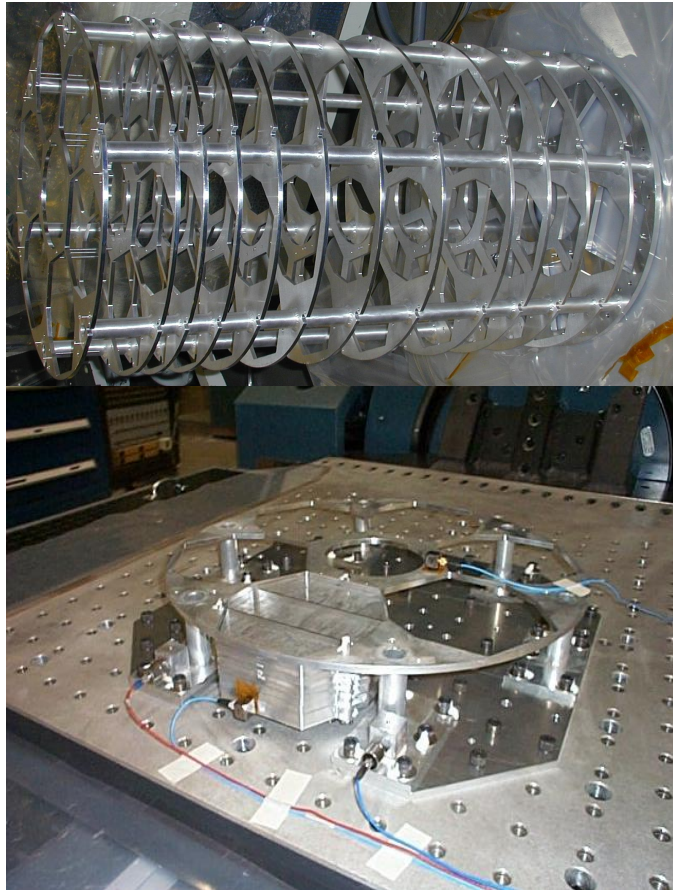
Figure 8: In the upper left is a picture of the actual collimator assembly. On the right, students mount the assembly onto the alignment fixture and begin aligning the collimator plates. The lower left shows the test unit on the shake table at Ball Aerospace.

4.3 Off-plane grating array

The gratings will deliver high dispersion, high efficiency and low aberration spectroscopy. A single grating cannot efficiently disperse the entire converging beam. Therefore, the gratings will be arranged in an array immediately following the collimator in the optical path as shown in figure 5. This will not only maximize the collecting area but will also maintain a low graze angle across the entire beam. Such an array is only feasible in the off-plane mount. When gratings are placed close to one another in an array, the in-plane mount will diffract light into inside orders that are vignetted by adjacent gratings thus decreasing the efficiency. This is not the case for the off-plane mount where light is dispersed into a cone with a shallow half angle equal to the graze. Furthermore, at graze angles an in-plane blazed grating will have decreased efficiency due to groove shadowing, which is solved by going to the off-plane configuration. Finally, the dispersion in the off-plane mount is extremely constant and completely independent of the graze angle (0.88 Å/mm in first order for this payload). This is a crucial component when performing high resolution spectroscopy on objects that cover large solid angles because the spectral lines will not distort over the range of angles but just lengthen. The in-plane mount has a non-linear distribution on the focal plane thus hindering the high resolution capabilities.

HORIBA Jobin-Yvon, Inc. (JY) has an existing master that will work for our application. The master has sinusoidal grooves at a density of 5670grooves/mm and is 104mm x 104mm thus setting one dimension of the payload grating size. However, to decide on the dimension along the grooves we used a simple rule of thumb. Given a throw of 2m, to keep resolution at 100 ($\lambda/\Delta\lambda$) the groove length should be 2m/100 or 20mm. Therefore, the gratings were chosen to be 104mm wide with a 20mm groove length. Using the limitations set by module packaging as well as detector packaging, the graze angle was chosen to be 4.4°. A 20mm grating at 4.4° gives only a 1.53mm effective length. Therefore, in order to maximize the throughput of the grating array, the grating substrates must be extremely thin to minimize the amount of light they block. We researched many possible materials and ultimately decided that thin metal would be the best choice as it is inexpensive and quick to obtain. Thin Metal Parts has made our substrate plates by depositing

electroformed nickel onto a flat (~λ/2) stainless steel mandrel. They were able to obtain a thickness of 0.005±0.0003". After accounting for this thickness we will require 67 gratings per module to catch the light in a 104mm x 104mm array.

JY has completed a thin substrate grating replication study and has developed a method of producing high quality thin replicas onto the electroformed nickel substrates. Due to the size of the replicas, each will need to be cut into 5 pieces thus requiring at least 26 replicas for the two modules. We researched several cutting techniques but only one was found suitable for this application. The novel laser cutting process will be done by IMRA America, Inc and involves femtosecond pulsed lasers that cut through the epoxy layer of the gratings without raising its temperature thus eliminating delamination of the grating layers and providing us with gratings free of any defects. Finally, the gratings are coated with electroless nickel which offers 30%-75% reflectivity at this angle over the 40Å-120Å (first order) payload bandpass. This coating will also reduce thermal bimetallic bending since the substrates are nickel as well.

The thinness of the gratings and their flatness requirements present a significant mounting challenge. Analysis showed that under vibration the gratings would have too low a fundamental frequency giving a maximum displacement greater than their spacing[19]. In order to achieve a resolution of 100, the gratings must be flat to within one part in 2000 along their length. To this end, a grating mount was designed which pulls the gratings from each end and holds them in tension. Thus, the flexure mount was made of titanium with a spring mechanism to hold each grating at a tension of 5 lbf to increase the fundamental frequency. The mount was taken through two engineering test units to achieve the appropriate tolerances. The second engineering unit with 6 gratings bonded in place is shown in figure 9. We developed a flatness testing bench, using a HeNe laser across the length of several of the gratings to show that this mount holds flatness to within tolerance.
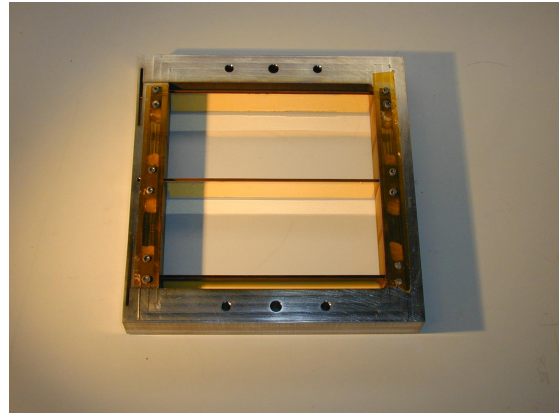

Figure 9: The second engineering test unit for the off-plane grating array mount flexure.

4.4 Detectors

For the detector we have chosen to use a Gas Electron Multiplier (GEM), which is currently being built by Sensor Sciences LLC (figure 10). This innovative detector uses a gas filled chamber segmented by perforated kapton film coated with a conductive layer on each side. The perforation holes provide a potential difference through which the electron cloud is accelerated resulting in a gain. The counters are capable of 200μm spatial resolution, $>10^5$ counts/sec and <1μsec time tagging. Since our spectral lines are ~1.2mm in width the detector will be capable of oversampling the point spread function. Furthermore, the count rate is ample for our X-ray observation. One of the most attractive features of such a detector is that they can be made with very large formats, which is essential due to the system's dispersion and line lengths. The entrance window is a 10cm × 10cm polyimide window that's 3500Å thick to maximize transmission while maintaining integrity. A 100Å carbon coat is added for conductivity. Due to the thinness, a grid bar and mesh support system is applied. The transmission of the mesh and frame is 57.8% given a 20lines/in stainless steel mesh. The counter gas is 75% Ar with a balance of CO_2 to give us good quantum efficiency at the desired energies. The thickness of the

Figure 10: GEM detector on a test bench.

window gives a leak rate of ~0.1-1%/hr and a burst pressure of ~3atm. We will operate a gas flow system that maintains an operating pressure of 1 atm. This system also counteracts the leak rate and compensates for micro tears in the window in order to achieve gain stability. A small x-ray source, 4μCurie Fe55, is incorporated at each detector to serve as a calibrator and to monitor gain fluctuations during flight. The sources have been acquired from the University of Colorado Department of Environmental Health and Safety and cleared through Wallops Flight Facility. They are mounted in a lead tube fixture to the corner of each of the detectors. Finally, the anode is a serpentine cross delay line.
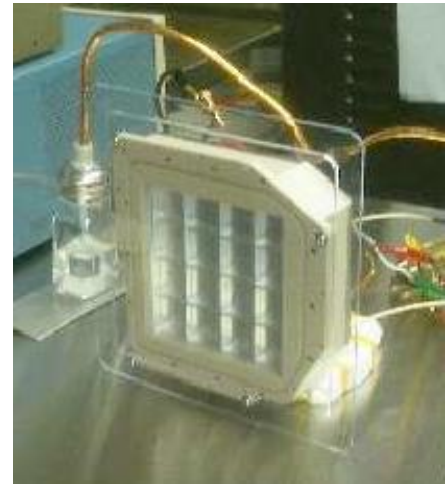
The output of the resistive anode is analyzed by a custom electronics system. Similar systems were previously used to analyze the output of micro-channel plate resistive anode systems that have flown over a dozen times.
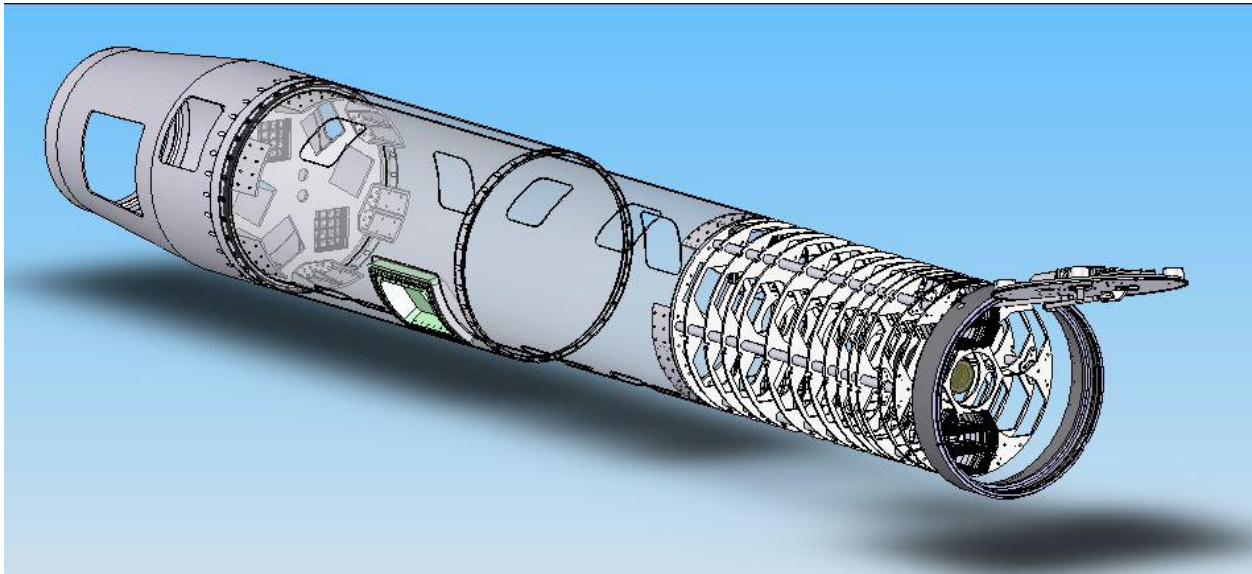
4.5 Component integration

Figure 11: Overall payload design and component layout.

The overall design for CYXESS is complete and its current state is shown in figure 11. The SolidWorks assembly shows the shutter door through to the electronics section. There are 6 aluminum tubes running through the collimator plates for support. The collimator plates are welded to the tubes forming a solid structure. The grating array will be mounted to the final plate of this solid structure to another specialized plate that closely resembles the collimator plates. The entire structure is cantilevered off the detector bulkhead using an interior support structure. Since it is cantilevered, the third collimator plate is bumpered against the rocket skin giving additional support. We are in the process of aligning the collimator plates to the skeleton plates. Wallops Flight Facility is currently fabricating the interior support structure and detector bulkhead. Once in house we will begin final alignment and assembly.
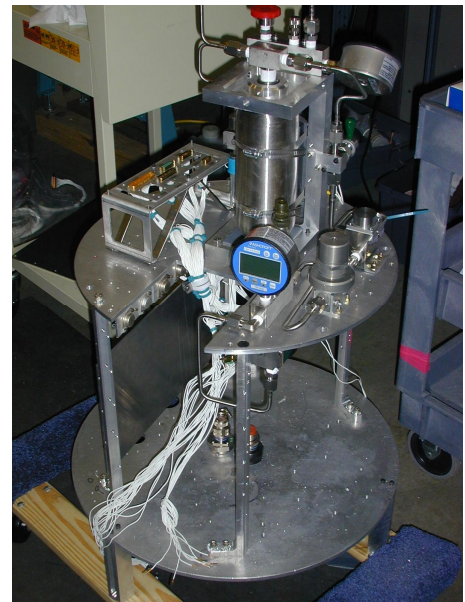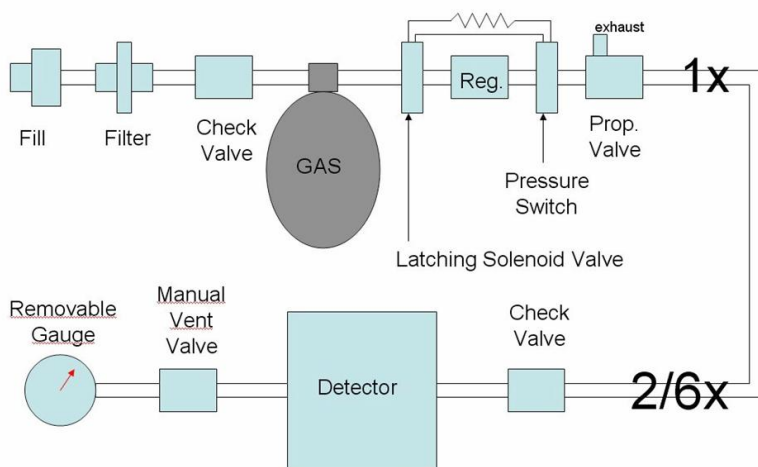

Figure 12: On the left is a schematic of the gas system and the picture on the right shows the fabricated gas system in the transition section of the payload.

Figure 12 gives a closer look at the gas/electronics section. The schematic gives an overview of the gas system used to stabilize the detectors. It begins with a fill system for the reusable gas container. Then, a pressure switch is incorporated to close a latching solenoid valve if the regulator fails. Following this is a proportional valve that creates a smooth flow of gas downstream and provides us with a downlink during flight. These components form the singular front end of the system with separate detectors branching off from here. Each detector system consists of a check valve that prevents backflow of gas out of the detector if the front end pressure should fall for any reason, the detector itself, a manual vent valve that is open only to purge the detector, and a removable gauge that will be used on the ground to monitor detector pressure. The gas system components have all been fabricated and procured. It is currently undergoing testing, leading up to integration with the detectors (figure 12).
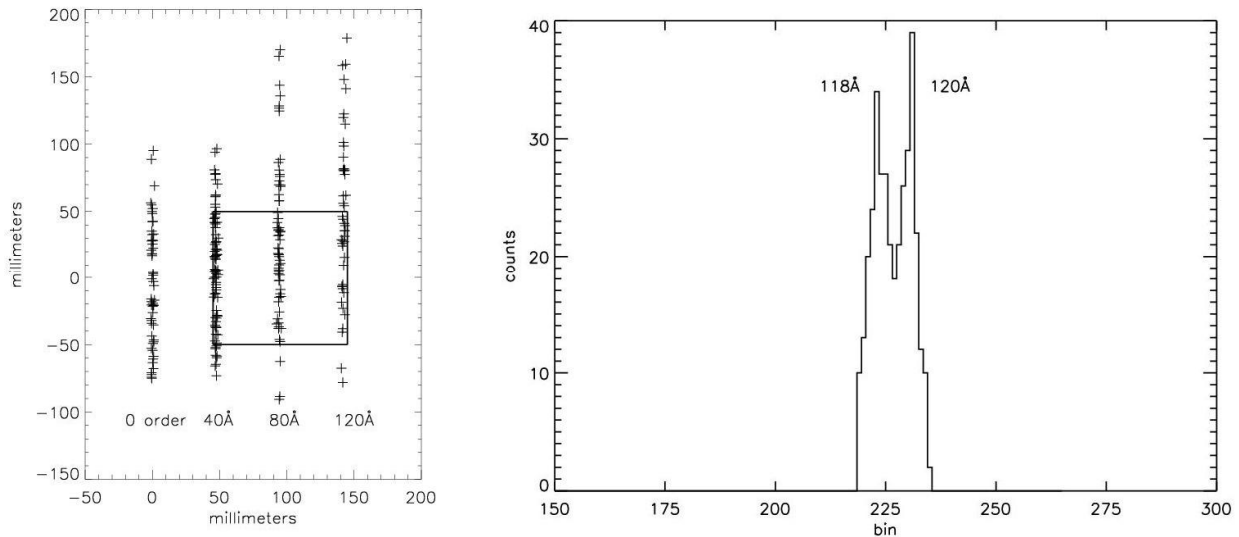
5. PERFORMANCE

Figure 13: On the left is a raytrace of the spectrum at the focal plane. The square indicates the position and size of the detector face. On the right is a raytrace of two spectral lines showing a resolution around 100.

The spectral resolution is limited by the dispersion of the gratings. We have raytraced the system to determine its spectral resolution as shown in figure 13. On the left we see a series of vertical lines. The line to the left is the zero order image through the collimator and reflected off the gratings. The lines to the right are spectral lines every 40Å up to 120Å, showing the pattern and the conical diffraction. The lines are quite long because there are no constraints in that dimension. However, the detector still catches >65% of the dispersed light. Also, due to the nature of a diffuse source, the line broadens somewhat after leaving the collimator, but the width of the dispersed lines keeps the ~1.2mm width of zero order, indicating dispersion limitation, not aberration.   In the right panel we have chosen two wavelengths, 118 and 120Å. They are cleanly split, indicating spectral resolution ($\lambda/\delta\lambda$) greater than 100.
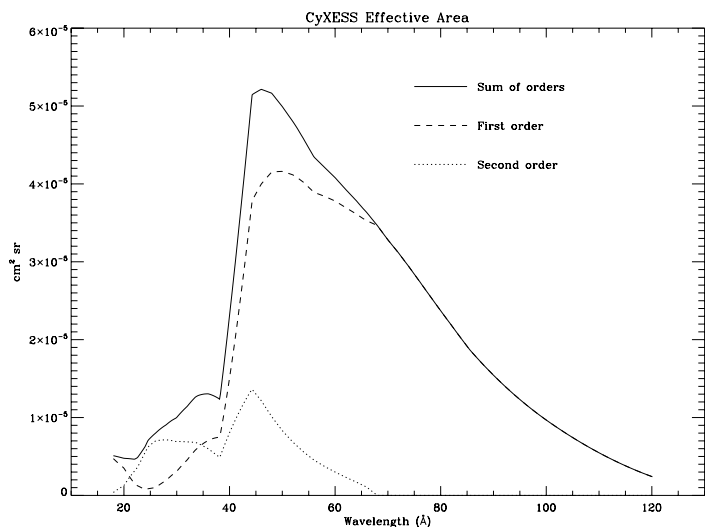

Figure 14: Effective area curve for CyXESS in 1st, 2nd and sum of orders

The other major performance specification is the system sensitivity. The event rate for radiation is set by the effective area which is given in units of $cm^2 deg^2$, since the signal increases with both solid angle and collecting area. For this design concept, the collecting area is the size of the zero order image on the focal plane. The solid angle is given by the effective solid angle that each point in the focal plane can view on the sky. The effective area curve for first order, second order and the sum of orders is given in figure 14. This model area has been taken through 2 modules with $1.2cm^2$ of area, the efficiency curves for the gratings in two orders, the transmission curve for the polyimide window and the mechanical throughput of the window support structure (57.8%). Furthermore, instead of using the entire sky coverage of the Cygnus Loop we only considered those areas contributing to the flux in our bandpass. It has been shown that the emission comes from an annulus of 4' at a 1.43° radius giving 0.614sqdeg of emission as opposed to the 10sqdeg field of view of the payload[6,9].

Figure 15 displays a spectrum of the Cygnus Loop as viewed by our payload. The model spectrum used is shown on top. This CyXESS model was created by averaging an x-ray spectrum of Cygnus Loop emission as seen with Chandra[9] with a spectrum as seen by ROSAT[6]. Since these spectra were broadband, they were used as guidelines for the total flux. In order to simulate the emission lines that would be present we used a spectrum of the soft X-ray background as seen by the Diffuse X-ray Spectrometer[20]. These lines were scaled up to what they would be for Cygnus and averaged with the Chandra/ROSAT averaged spectrum. The two oxygen lines (5% of the total emission[21], 3.75% in OVII and 1.25% in OVIII[22]) were added to the model which was then renormalized to the total counts as expected from Chandra/ROSAT. This model was convolved with the CyXESS payload in the following way: there are 2 modules, 300 seconds of observing time, and the effective area curve from above. The counts total 685. The bottom plot shows a data simulation using Poisson statistics based on the calculated count rate.

The payload will be calibrated using the same facilities here at the University of Colorado that we have been using to analyze test gratings for the Constellation-X mission and have used many times in the past to calibrate rocket payloads. The payload will be placed in our long rocket calibration vacuum chamber and a pencil beam source will be used to scan across the field of view. This will simulate the various angles expected from our field of view allowing us to test the efficiency of the collimator, to align the grating arrays, to simulate spectral lines from the gratings and to test the efficiency, electronics and gas flow system of the detector.

For the subsequent launch of the payload we will be able to incorporate up to 6 of the above modules to obtain enough signal for an observation of the X-ray background. As calculated from the current payload

Figure 15: A CyXESS model spectrum and data simulation.

configuration, the observation of the background will yield a total of ~420 counts in the spectrum, a 40% improvement over previous spectra. This initial launch will provide a proof-of-concept trial on these modules that will allow us to maximize their efficiency to achieve a larger total count and higher resolution spectrum.
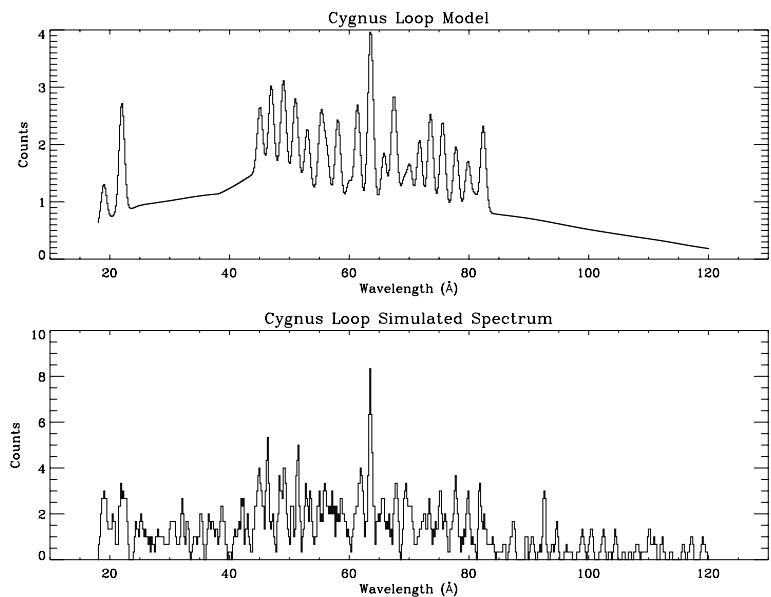
6. CONCLUSION

We have designed and are currently fabricating a new sounding rocket payload that will perform high resolution (R~100), x-ray spectroscopy of diffuse celestial x-ray sources. The instrument features a new geometry that allows for high resolution along with high throughput. A wire-grid collimator constrains light from diffuse sources into a converging beam that feeds an array of diffraction gratings in the extreme off-plane mount and ultimately a GEM

detector. The first launch will occur on Sept. 7th, 2006 and will concentrate on the Cygnus Loop supernova remnant. CyXESS will be the first instrument to provide a high resolution spectrum in the soft X-ray bandpass. The spectrum will be dividable into contributions from the two temperature regions, the cloud shock and the reflected shock, which both originate from the interaction of the blast wave with clouds. In addition, the high spectral resolution will allow us to employ nonequilibrium model fits, which will determine electron temperature, column density, emission measure, ionization parameter and abundance determinations of elements such as O, Si, Fe, Ne and Mg. The fits will be more exact and allow a stricter constraint on the variables. The abundant number of lines achievable with this resolution will be indicative of many temperature ranges. By calculating the emission measure for each line, we will be able to estimate the emission measure as a function of temperature for the entire remnant.

ACKNOWLEDGEMENTS

REFERENCES

1. Fesen, R.A., Blair, W.P., & Kirshner, R.P. 1982, ApJ, 262, 171
2. Blair, W.P. & Sankrit, R. 2005, AJ, 1129, 2268
3. McCray, R., & Snow, T.P. Jr. 1979, ARA&A, 17, 213
4. McEntaffer, R.L., Cash, W., Shipley, A., "Sounding rocket payload development for X-ray observations of the Cygnus Loop" 2005, *Proc. Soc. Photo-Opt. Instr. Eng.*, 5900, 393-404.
5. Vedder, P.W., Canizares, C.R., Markert, T.H & Pradhan, A.K. 1986, ApJ, 307, 269
6. Levenson, N.A., Graham, J.R., & Snowden, S.L. 1999, ApJ, 526, 874
7. Ku, W.H.M., Kahn, S.M., Pisarski, R. & Long, K.S. 1984, ApJ, 278, 615
8. Miyata, E. & Tsunemi, H. 2001, ApJ, 552, 624
9. Levenson, N.A., Graham, J.R., & Walters, J.L. 2002, ApJ, 576, 798
10. Cash, W. "X-ray optics. 2: A technique for high resolution" 1991 *Applied Optics*, 30, 1749-1759
11. Catura, R., R. Stern, W. Cash, D. Windt, J.L. Culhane, J. Lappington, K. Barnsdale, "X-ray Objective Grating Spectrograph" 1988 *Proc. Soc. Photo-Opt. Instr. Eng.*, 830, 204-216
12. Cash, W., "Echelle spectrographs at grazing incidence" 1982 *Appl. Opt* , 21, 710
13. Neviere, M., D. Maystre, W.R. Hunter, "On the use of classical and conical diffraction mountings for XUV gratings" 1978 *JOSA*, 68, 1106-1113
14. W. Werner, "X-ray efficiencies of blazed gratings in extreme off-plane mountings" 1977, *Applied Optics*, 16, 2078-2080
15. Goray, L.I., "Rigorous efficiency calculations for blazed gratings working in in- and off-plane mountings in the 5-50Å wavelength range" 2003, *Proc. Soc. Photo-Opt. Instr. Eng*, 5168, 260-270
16. McEntaffer, R.L., Osterman, S.N., Cash, W.C., Gilchrist, J., Flamand, J., Touzet, B., Bonnemason, F., Brach, C., "X-ray performance of gratings in the extreme off-plane mount" 2003, *Proc. Soc. Photo-Opt. Instr. Eng.*, 5168, 492-498
17. Osterman, S.N., McEntaffer, R.L., Cash, W.C., Shipley, A., "Off-plane grating performance for Constellation-X", *Proc. Soc. Photo-Opt. Instr. Eng.*, 5488, 302-312.
18. Heilmann, R. et al 2004, *Proc. Soc. Photo-Opt. Instr. Eng.*, 5168, 271
19. Shipley, A., McEntaffer, R.L., Cash, W., "Foil reflection grating mount for diffuse x-ray spectroscopy" 2005, *Proc. Soc. Photo-Opt. Instr. Eng.*, 2005, 5900
20. Sanders, W.T., Edgar, R.J., Kraushaar, W.L., McCammon, D., Morgenthaler, J.P. 2001, ApJ, 554, 694
21. Stark, J.P.W. & Culhane, J.L. 1978, MNRAS, 184, 509
22. McCammon, D., Almy, R., Apodaca, E., Bergmann Tiest, W., Cui, W., Deiker, S., Galeazzi, M., Juda, M., Lesser, A., Mihara, T., Morganthaler, J.P., Sanders, W.T., Zhang, J., 2002, ApJ, 576, 188.